Nanoscale

PAPER

View Article Online
View Journal | View Issue

Check for updates

Cite this: *Nanoscale*, 2026, **18**, 307

Enhancing colloidal stability of anisotropic magnetic nanodiscs through mesoporous silica and P(NIPAM/MAA) copolymer coatings

P. Rafael Donnarumma, [a,b] Micaela A. Macchione, [a,c] Franziska Wasner,[d] Elif Kocar,[d] Vicente Durán Toro,[d] Santiago Marzini Irranca, [e,f] Eduart Gutiérrez Pineda, [a] Sunisa Thongsom, [a] Danijela Gregurec *[d] and Sergio E. Moya *[a,g]

Magnetic nanodiscs (MNDs), a class of anisotropic magnetite nanomaterials, have attracted considerable attention in smart actuation as they can generate heat through hysteretic losses and their discoidal shape can be tuned to exhibit vortex magnetization and generate mechanical stimuli. Despite near-zero net magnetization, at high concentrations, interparticle forces become dominant leading to MND aggregation. Here, we have optimized a previously reported synthetic approach based on the synthesis of hematite templates subsequently converted into a magnetite phase. We show that removal of oleic acid (OA) during the reduction step results in the same colloidal stability as in the presence of OA but avoids erosion of the MNDs associated with OA. We introduce a thin mesoporous silica coating on the surface of hematite, effectively diminishing aggregation during reduction while allowing complete conversion into magnetite. This silica layer facilitates subsequent silane chemistry and the grafting of poly(*N*-isopropylacrylamide-*co*-methacrylic acid) P(NIPAM/MMA) coatings with 80 : 20 and 50 : 50 ratios, yielding highly stable aqueous suspensions of MNDs, both in aqueous and cell culture media. These findings establish a versatile pathway toward colloidally stable MNDs, thereby broadening their applicability in biomedical research.

Received 10th September 2025,
Accepted 5th November 2025

DOI: 10.1039/d5nr03822g

rsc.li/nanoscale

Open Access Article. Published on 01 December 2025. Downloaded on 4/5/2026 1:17:45 AM.
This article is licensed under a Creative Commons Attribution-NonCommercial 3.0 Unported Licence.

Introduction

Anisotropic Magnetic Materials (AMMs), such as nanodiscs, nanorods, and nanotubes, have recently gained considerable scientific attention due to their multiple possibilities as smart materials and their promising applications in biomedicine, particularly in areas like neuromodulation.[1,2] Magnetic materials can respond to external magnetic fields by generating heat through hysteretic losses in frequencies of hundreds of kilohertz. This heat has been applied to eradicate tumours in the so-called magnetic hyperthermia technique.[3–6] This property can also be exploited for wireless magnetothermal deep brain stimulation at optimal heat dissipation temperatures.[7] Furthermore, the anisotropic shape of AMMs allows them to trigger mechanical stimulation through torque on mechanosensory cells under slower, 1–10 Hz magnetic fields, when ground vortex magnetization in a specific geometric aspect ratio aligns in plane with the direction of the magnetic field.[8]

Among AMMs, magnetic nanodiscs (MNDs) are particularly suited for mechanical stimulation, as the piconewton scale torques demonstrated efficient modulation of the activity in mechanosensory cells.[8] Magnetomechanical activation of the mechanosensitive cation channel TRPV4, heterologously expressed in non-mechanosensitive HEK293 cells, confirmed that the stimulation is mediated through mechanosensitive ion channels.

Because magnetite has an inverse spinel lattice that favors isotropic growth, AMMs are typically obtained through the chemical reduction of non-magnetic hematite (α-Fe_2O_3) templates with a hexagonal lattice to magnetite (Fe_3O_4).[3,5,9] The

[a]*Soft Matter Nanotechnology Group, CIC biomaGUNE, Basque Research and Technological Alliance, San Sebastian, Spain. E-mail: smoya@cicbiomagune.es*
[b]*Departamento de Química Aplicada, Universidad del País Vasco UPV/EHU, Leioa, Bizkaia, Spain*
[c]*CONICET, Centro de Investigaciones y Transferencia de Villa María (CIT Villa María), Villa María X5900LQC, Argentina*
[d]*Biointerfaces Lab, Department of Chemistry and Pharmacy, Friedrich-Alexander Universität Erlangen-Nuremberg, Erlangen, Germany. E-mail: danijela.gregurec@fau.de*
[e]*Departamento de Química Orgánica, Facultad de Ciencias Químicas, Universidad Nacional de Córdoba, Ciudad Universitaria, Córdoba, Argentina*
[f]*Instituto de Investigación y Desarrollo en Ingeniería de Procesos y Química Aplicada (IPQA-CONICET), Córdoba, Argentina*
[g]*Department of Biochemistry, Faculty of Medicine, Chulalongkorn University, Bangkok 10330, Thailand*

Open Access Article. Published on 01 December 2025. Downloaded on 4/5/2026 1:17:45 AM.
This article is licensed under a Creative Commons Attribution-NonCommercial 3.0 Unported Licence.

crystal structure of hematite allows for directional growth, leading to well-defined anisotropic morphologies.[10]

Hematite nanoparticles can be synthesized with diverse exposed facets, resulting in distinct morphologies such as rhombic cubes, hexagonal platelets or discs, and hexagonal bipyramids.[11,12] Due to the aggregation that may take place during synthesis and reduction to magnetite, further efforts are still required to develop synthesis strategies and surface functionalization towards enhancing their colloidal stability.

A well-established strategy to stabilize inorganic nanomaterials that otherwise form unstable colloidal dispersions in water is to coat them with silica.[13] Silica coatings are widely employed not only to enhance the colloidal stability of core materials but also because they can be readily functionalized *via* silanization with a broad range of molecules, including polymers that further improve stability and biocompatibility.[14]

In the case of magnetic nanomaterials, silica coatings additionally serve as barriers between individual nanoparticles, reducing their magnetic interactions. Besides deposition of a dense, hard silica shell on inorganic nanoparticles, it is also possible to grow a permeable mesoporous silica layer, which confers similar benefits to those of a hard shell while introducing pores and channels that prevent complete isolation of the core from its surrounding medium.[15]

This manuscript presents an optimized synthetic strategy for producing MNDs, as schematized in Fig. 1, focusing on modifications to the reduction process that preserve a uniform nanodisc morphology, minimize aggregation, and enhance colloidal stability with the ultimate goal of advancing their biomedical potential while maintaining their unique properties. We demonstrate that some functionalization steps commonly used in MND synthesis are not necessary for the stabilization of the MNDs in aqueous media and that the coating of hematite with mesoporous silica prevents aggregation of the nanoparticles during reduction, while the pores of the silica coating allow the reducing agents to reach the hematite core and carry out a 100% conversion of the hematite core to magnetite.[16–18] In addition, the silica coatings facilitate further functionalization of MNDs through silane chemistry, allowing the grafting of polymers around the MNDs that provide additional stability to the hybrid nanostructures.[19] Our results reveal that poly(*N*-isopropylacrylamide) (NIPAM) and methacrylic acid (MAA) coatings confer superior colloidal stability over time, both in water and in cell culture media.

Experimental section

Materials

All chemicals used in this work were of analytical grade and utilized as received without further purification. 3-(Trimethoxysilyl) propyl methacrylate (MEMO) (>97%), isopropanol (99.5%), sodium dodecyl sulfate (SDS) (>99%), *N*,*N*,*N*′,*N*′-tetramethylethylenediamine (TEMED) (>99%), ammonium persulfate (APS) (99%), *N*-isopropylacrylamide (NIPAM) (97%), methacrylic acid (MAA), $FeCl_3{\cdot}6H_2O$ (97%), tri-*n*-octylamine (TOA) (98%), oleic acid (OA) (90%), tetraethyl orthosilicate (TEOS) (98%), and hexadecyltrimethylammonium bromide (CTAB) (>99%) were purchased from Sigma-Aldrich. NH_4OH solution (25% in water) and toluene (>99.7%) were purchased from Fisher. Anhydrous sodium acetate (>99.0%) was purchased from Merck. Absolute ethanol was purchased from Scharlau. RPMI 1640 solution was purchased from HyClone. H_2 (100%) was provided by Carburos Metálicos.

Methods

Hematite and magnetite nanodisc synthesis. Magnetite nanodiscs were produced using a two-step process in which hematite (α-Fe_2O_3) nanodisc templates are hydrothermally fabricated and subsequently reduced *via* a hydrogen-wet reduction method.[3,8]

In the first step, α-Fe_2O_3 nanodiscs were synthesized by mixing 0.273 g of $FeCl_3{\cdot}6H_2O$ and 0.8 g of anhydrous sodium acetate in a solution of 10 mL of absolute ethanol and 1 mL of Mili-Q H_2O inside a Teflon-lined steel vessel. The reaction mixture was homogenized through stirring. The Teflon-lined vessel was then heated to 180 °C for 18 h. The red α-Fe_2O_3 nanodiscs were cooled down to room temperature, centrifuged, and washed three times with deionized (DI) H_2O and three times with ethanol to remove unreacted reagents; finally, they were left to air dry for further reduction.

In the second step, α-Fe_2O_3 nanodiscs were reduced to magnetite (Fe_3O_4) by dispersing the hematite in 20 mL of TOA and homogenized by ultrasound for 10 min. The mixture was placed in a three-neck flask with an overhead stirrer with Teflon palettes and fluxed at 360 °C in an atmosphere of H_2 (100%) for 30 min until it changed its color from red to black. Once cooled, the Fe_3O_4 nanodiscs were washed several times with ethanol and then left to air dry.

Mesoporous silica coated magnetite nanodiscs. To obtain mesoporous silica coated magnetic nanodiscs, a mesoporous

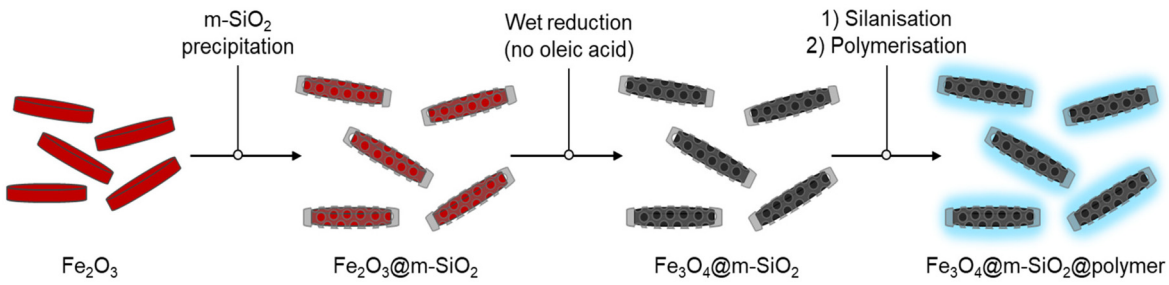

Fig. 1 Scheme of the fabrication of polymer/mesoporous silica-coated magnetite nanodisc hybrid nanostructures.

This journal is © The Royal Society of Chemistry 2026

Open Access Article. Published on 01 December 2025. Downloaded on 4/5/2026 1:17:45 AM.
This article is licensed under a Creative Commons Attribution-NonCommercial 3.0 Unported Licence.

silica layer was deposited on α-Fe_2O_3 nanodiscs before the reduction step adapting a protocol from the literature.[8] Four different conditions were tested varying the TEOS amount and the isopropanol : water ratio, while keeping the CTAB and base concentrations constant. For this, 5 mg of α-Fe_2O_3 nanodiscs and 40 mg of CTAB were put in a mixture of isopropanol and DI H_2O, and 0.125 mL of NH_4OH 25% was added. This solution was sonicated in a bath for 5 min. The resultant dispersion was ultrasonicated with a tip-probe ultrasonicator for 10 min at room temperature, at 40% amplitude (VCX 500, 500 W). Parallelly, 4 μL of TEOS was pipetted into 1 mL of isopropanol.

Half of the TEOS solution was added to the α-Fe_2O_3 solution in a sonication bath. The mixture was ultrasonicated with the tip-probe ultrasonicator for 30 min in an ice bath to control the temperature. The rest of the TEOS solution was added and then the mixture was ultrasonicated for 30 min more. The α-Fe_2O_3@m-SiO_2 was centrifuged and washed twice with a washing solution (50% 0.5 M HCl, and 50% ethanol) and three times with ethanol; finally, it was left to air dry overnight. The reduction proceeded in the same way as for uncoated α-Fe_2O_3 to produce Fe_3O_4@m-SiO_2.

Surface modification of Fe_3O_4@m-SiO_2. The surface functionalization of the MNDs was carried out *via* silanization using MEMO. Briefly, 1 mg of Fe_3O_4@m-SiO_2 was suspended in 10 mL of toluene and ultrasonicated in an ice bath for 10 min. Then, 2 mL of MEMO was added, and the resulting dispersion was ultrasonicated for 30 min at 70 °C. The reaction mixture was washed three times with isopropanol to remove unreacted species. Finally, the Fe_3O_4@m-SiO_2@MEMO particles were dried to obtain a powder.

Synthesis of polymeric coatings on Fe_3O_4@m-SiO_2. The synthesis of polymeric coatings was carried out following a previously reported protocol, consisting of a free radical precipitation/dispersion polymerization assisted by ultrasonication, with some modification.[20] First, 0.1 mg of Fe_3O_4@m-SiO_2@MEMO were weighed and resuspended in 3 mL of water. In a separate vial, NIPAM was weighed and dissolved in 5 mL of water. The Fe_3O_4@m-SiO_2@MEMO suspension was ultrasonicated for 2 min, and the NIPAM solution was then added, followed by the addition of MAA, keeping the total monomer amount at 1 mmol; and SDS (0.6 mM) was subsequently added to the reaction flask. Finally, solutions of TEMED (0.075 mmol) and APS (0.015 mmol), used as the catalyst and initiator, respectively, were injected along with Milli-Q water to reach a final volume of 10.0 mL. The reaction mixture was then ultrasonicated at 70 °C using a tip-probe ultrasonicator for 15 min at 40% amplitude. The mixture was allowed to cool slightly and then subjected to 10 min of ultrasonication in an ice bath to achieve final stabilization of the system. Three different polymer compositions were produced by varying the monomer composition and ratios: pure PNIPAM (Fe_3O_4@m-SiO_2@P1), and copolymers of NIPAM and MAA (P(NIPAM-*co*-MAA)), at 80 : 20 (Fe_3O_4@m-SiO_2@P2) and 50 : 50 (Fe_3O_4@m-SiO_2@P3).

***In vitro* cytotoxicity studies.** The normal human fibroblast WI-38 cell line and normal HEK-293T (American Type Culture Collection (ATCC), Manassas, WV, USA) were used to test the biocompatibility of Fe_3O_4@m-SiO_2 and Fe_3O_4@m-SiO_2@P3. HEK-293T cells were cultured in high glucose Dulbecco's Modified Eagle's Medium (DMEM), and WI-38 were cultured in Minimum Essential Medium (MEM); both media were supplemented with GlutaMAX™ (Gibco/Thermo Fisher Scientific, Waltham, MA, USA), with 10% fetal bovine serum (FBS, Gibco), 1% penicillin/streptomycin solution (Gibco) and incubated in a humidified incubator at 37 °C with 5% CO_2. Cells were seeded at a density of 1 × 104 cells per well in 96-well plates (total 100 μL per well) overnight. Cells were subsequently treated with various concentrations of Fe_3O_4@m-SiO_2 and Fe_3O_4@m-SiO_2@P3 (0–200 μg mL^{-1}) for 24 and 48 h (total 200 μL per well) and finally cell viability was determined using the MTS assay. In short, before detection, 40 μL of MTS solution was added to the well (CellTiter 96® AQueous One Solution Cell Proliferation Assay, Promega #G3580), incubated in a CO_2 incubator for 3 hours, and its optical density was measured at 490 nm. Cell viability was calculated using the following equation:

$$\text{Cell viability}\,(\%) = \frac{\text{OD}_{490\,\text{treatment}}}{\text{OD}_{490\,\text{control}}} \times 100$$

where OD_{490} stands for the optical density at 490 nm for treated samples (with Fe_3O_4 nanodiscs) and control (without nanodiscs).

Characterization. Transmission electron microscopy (TEM) micrographs were obtained on a Zeiss LEO912 microscope at an 80 keV acceleration voltage. Samples were prepared by drop casting 1 μL of a diluted dispersion of the nanoparticles in ethanol on a 400 mesh copper carbon support film. For the observation of the mesoporous structure of the silica coating, ultrathin C films on lacey carbon grids were used. The size distribution and thicknesses were determined from populations of around 300 particles by using ImageJ software.

Scanning electron microscopy (SEM) images were obtained with a field-emission scanning electron microscope (FE-SEM; JSM-IT800HL, JEOL, Tokyo, Japan) in combination with an EDX detector (Oxford INCA). Samples were prepared the same way as for TEM.

Atomic force microscopy (AFM) was used to analyse the sample's morphology in a Multimode 8HR (Bruker). Samples were resuspended in a water : methanol solution and spin-coated (20 μL) onto a freshly cleaved mica surface and allowed to dry. Images were captured using a conventional tapping mode with a TESP-V2 probe (Bruker). The data were processed with Nanoscope 2.0 software (Bruker).

X-ray diffraction (XRD) was performed between 10 and 80 (2θ) degrees using a Bruker D8 Advance diffractometer equipped with a Lynxeye XE-T detector using Cu Kα radiation (1.5406 Å). Phase identification was done by comparing the diffraction pattern to the simulated diffractions of Fe_2O_3 and Fe_3O_4. Infrared spectra were obtained using a Bruker Invenio-X Fourier transform infrared (FTIR) spectrometer by the accumulation of 64 scans over the 400–4000 cm^{-1} range with a resolution of 4 cm^{-1}. Samples were suspended in ethanol and deposited onto a diamond crystal. The ethanol was allowed to evaporate before measuring.

Open Access Article. Published on 01 December 2025. Downloaded on 4/5/2026 1:17:45 AM.
This article is licensed under a Creative Commons Attribution-NonCommercial 3.0 Unported Licence.

X-ray photoelectron spectra (XPS) were recorded using an XPS VersaProbe III energy spectrometer. Al-Kα radiation of 1486 eV was used. Gaussian–Lorentzian functions were used to adjust data after baseline correction.

The hydrodynamic diameter (D_h) and zeta potential of particles were determined by dynamic light scattering (DLS) using a Zetasizer Advance Ultra (Red Label) from Malvern Panalytical equipped with a He–Ne laser (633 nm, nominal maximal power of 10 mW) as the light source. The scattered light was measured at an angle of 90° and collected using an autocorrelator. Samples were dispersed in the corresponding solvent at a concentration of 0.01 mg mL^{-1} and dispersed using ultrasound for 10 minutes before measuring at 25 °C. Measurements were carried out after allowing 5 min for sample equilibration, with three successive runs on each sample.

Room temperature hysteresis curves, which quantify magnetization saturation and coercivity, were generated using a superconducting quantum interference device SQUID magnetometer MPMS3 (Quantum Design) in a vibrating sample magnetometry (VSM) mode.

Results and discussion

Optimization of MNDs synthesis

We improved the synthesis of MNDs by streamlining the procedure to eliminate steps that may promote aggregation or induce detrimental morphology changes, thereby enhancing particle stability and ensuring uniform morphological distribution throughout the synthesis. We followed and adapted the two-step procedure for the synthesis of MNDs originally reported by Yang *et al.*[3] with size optimization of vortex MNDs as described by Gregurec *et al.*[8] Typically, α-Fe_2O_3 is hydrothermally produced in the presence of sodium acetate and ethanol to precipitate into disc-shaped nanoparticles. These templates are then converted into the Fe_3O_4 phase by a wet hydrogen reduction process at 60 °C using tri-*n*-octylamine (TOA) as solvent and oleic acid (OA) as a surfactant added to prevent nanoparticle coalescence during the reaction. Water, acetate and ethanol have been shown in the literature to be necessary to produce the anisotropic shape of the α-Fe_2O_3 templates, and the associated synthetic conditions and mechanisms have been duly studied.[21] By contrast, the role of the OA in the reduction step as an efficient stabilising agent for preventing coalescence or aggregation of MNDs in TOA has not been fully investigated. Moreover, it has been indicated that an unfavorable ratio of oleic acid to nanoparticles could lead to material degradation as the harsh conditions in the presence of OA erode the MNDs resulting in smaller magnetic particles.[3]

With the aim of simplifying the reduction reaction and avoiding damage to the anisotropic shape of the Fe_3O_4, we studied the reduction process in the absence of OA. For this purpose, two samples were fabricated, with and without OA, labelled Fe_3O_4@OA and Fe_3O_4 bare, respectively.

The interaction between carboxylate groups of OA and the surface of spherical magnetite nanoparticles has been previously studied by FTIR and XPS, revealing either adsorption or chemisorption of OA on the magnetite surface with a chelating effect, depending on the surface characteristics and morphology of the particles.[22] In the present study, FTIR spectra of samples with and without OA revealed that no significant differences were observed. Only weak bands corresponding to the symmetric and asymmetric stretching of coordinated carboxylate groups of oleic acid in Fe_3O_4@OA, were detected at 1407 cm^{-1} and 1554 cm^{-1}, respectively (Fig. 2a).[23] These results indicate a limited presence of OA on the particle surface.

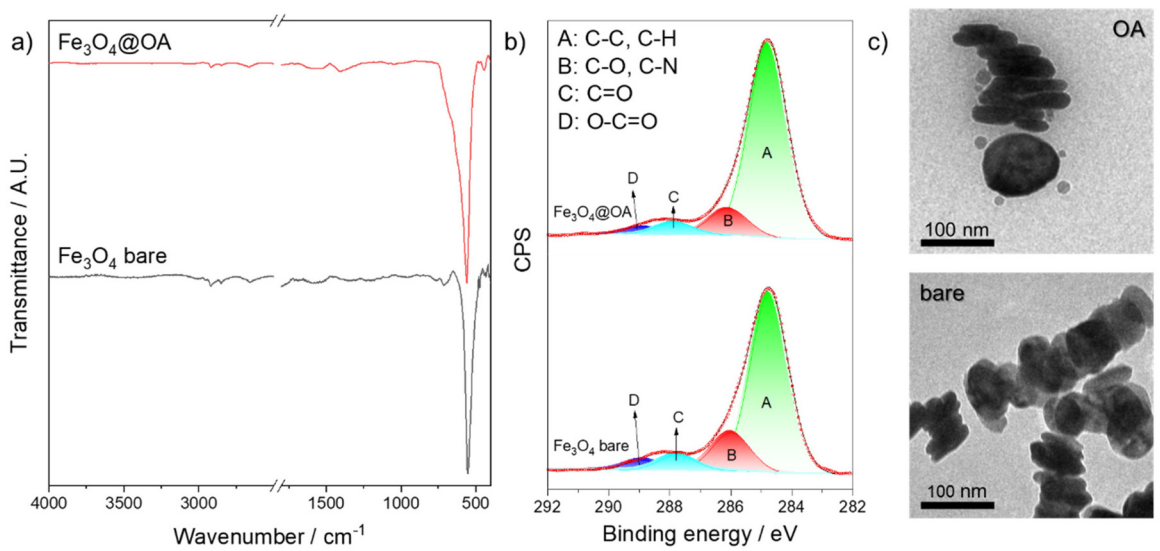

Fig. 2 Characterization of Fe_3O_4@OA and bare Fe_3O_4 by (a) FTIR, (b) XPS corresponding to the C 1s region, and (c) TEM (top: Fe_3O_4@OA; bottom: bare Fe_3O_4).

This journal is © The Royal Society of Chemistry 2026

Open Access Article. Published on 01 December 2025. Downloaded on 4/5/2026 1:17:45 AM.
This article is licensed under a Creative Commons Attribution-NonCommercial 3.0 Unported Licence.

XPS analysis also shows no detectable differences between the spectra of the two samples that would indicate the presence of surface OA. The C 1s signal intensity is of the same order of magnitude in both cases, despite the longer carbon chain in OA compared to acetate (Fig. 2b), providing further evidence that only acetates are present in the OA-treated sample. DLS was employed to probe the colloidal stability of the suspensions in the presence and absence of OA. Although DLS analysis assumes spherical geometry, while the particles studied here are anisotropic, this remains a reasonable approach to study their behavior in suspension, including colloidal stability and aggregation. Measurements of MNDs in both organic media (ethanol) and water confirm that neither sample exhibits solvent preference, as shown by both intensity and number distributions (Table S1 and Fig. S1). Bare Fe_3O_4 shows hydrodynamic diameters of 524 ± 59 nm in ethanol and 538 ± 24 nm in water, whereas Fe_3O_4@OA exhibits 548 ± 52 nm in ethanol and 507 ± 14 nm in water.

Finally, TEM imaging reveals that after reduction in the presence of OA, smaller spheres are formed in addition to MNDs (Fig. 2c). In contrast, bare Fe_3O_4 maintains the desired MND morphology, without evidence of small spherical particle formation.

Mesoporous silica coating

DLS measurements show that the hematite nanodiscs in ethanol exhibit an average hydrodynamic diameter of 199 ± 2 nm, with a polydispersity index (PDI) of 0.12, whereas MNDs in the same solvent exhibit a significantly larger average diameter of 524 ± 59 nm and a PDI of 0.38 (Table S1). A similar trend is observed in water, indicating that hematite nanodiscs are better dispersed in both media than their magnetite counterparts, most likely due to the absence of magnetic interactions among them.

To mitigate these interactions during the reduction of hematite to magnetite, a mesoporous silica layer was grown on the hematite templates to act as a physical barrier, thereby reducing the interparticle magnetic coupling during the reduction process, when hematite is converted into magnetite. Mesoporous silica was selected over a hard (dense) silica shell because its interconnected pore network permits the diffusion of solvents and H_2 molecules through the pores. The α-Fe_2O_3 templates were treated with hexadecyltrimethylammonium bromide (CTAB) as a shape-directing agent and dispersant in a mixture of different ratios of water and isopropanol, in the presence of NH_4OH as a basic hydrolysing agent. The hematite templates (Fig. S2, a diameter of 107 ± 14 nm; a width of 26 ± 7 nm) were well dispersed with an ultrasound tip, after which half of the TEOS was added to initiate SiO_2 deposition, followed by ultrasonication for 30 min to allow SiO_2 formation. The remaining TEOS was then added, and the suspension was ultrasonicated for an additional 30 min to complete the growth of the SiO_2 shell. Four different conditions were tested for silica shell growth by varying the TEOS concentration and the isopropanol : water ratio, while maintaining the CTAB and base concentrations constant. Under three conditions, the TEOS amount was kept constant while the isopropanol : water ratio was varied (Table 1), while under the fourth condition, the TEOS concentration was diluted tenfold with the isopropanol : water ratio set at 1 : 1. The resulting mesoporous SiO_2 (m-SiO_2) coatings were characterized by TEM (Fig. S3). As reported in the literature, an increased water content accelerates TEOS hydrolysis, producing a thicker m-SiO_2 layer.[24] In contrast, when the water content was very low (less than 10% of the total volume), the silica layer was too thin to be resolved by TEM (conditions 1 and 2). Conversely, at high water fractions, excess TEOS led to the formation of thick m-SiO_2 layers encapsulating multiple nanodiscs (condition 3). Optimal conditions for coating of individual nanodiscs were achieved with an excess of water and reduced TEOS concentration (condition 4), yielding uniform m-SiO_2 coating of 6 ± 1 nm, determined by ImageJ analysis.

Table 1 Tested conditions for m-SiO_2 growth. All coatings were prepared with the same α-Fe_2O_3 concentration (1 mg mL^{-1}), and NH_4OH (25%) was kept at 0.025 mL mL^{-1} solution

Condition	Water : isopropanol	TEOS (μL mL^{-1} sol)
1	0 : 5	8
2	0.2 : 4.8	8
3	2.5 : 2.5	8
4	2.5 : 2.5	0.8

No difference in reduction time was observed between α-Fe_2O_3 and α-Fe_2O_3@m-SiO_2, with both samples being completely reduced after 30 min under a continuous flow of H_2 (100%) at 360 °C.

TEM images confirm that the m-SiO_2 shell remains structurally preserved after reduction, although the layer thickness decreases slightly to 4 ± 1 nm for Fe_3O_4@m-SiO_2. In both α-Fe_2O_3 and Fe_3O_4, the mesoporous nature of the silica shell is evident in the TEM images, with surfaces appearing rough and non-uniform, rather than smooth (Fig. 3a and b), consistent with the expected and the highly porous structure (Fig. S4).[25] Energy-dispersive X-ray spectroscopy (EDX) mapping performed at multiple positions across the nanodiscs further confirms that the m-SiO_2 layer is evenly distributed across both the α-Fe_2O_3 and Fe_3O_4 surfaces (Fig. S5 and S6).

Tapping-mode atomic force microscopy (AFM) was used to characterize the surface topography of Fe_3O_4 and Fe_3O_4@m-SiO_2 nanodiscs, with representative images and surface roughness profiles shown in Fig. S7. AFM analysis revealed that silica-coated MNDs exhibit increased density of valleys and ridges with a lower root-mean-square surface roughness (RMS) of 0.191 ± 0.030 nm compared to bare MNDs, with an RMS of 0.582 ± 0.105 nm. Moreover, Fe_3O_4@m-SiO_2 nanodiscs exhibit a well-ordered surface geometry characterized by a hexagonal platelet arrangement resembling a pore array, absent in uncoated MNDs, indicating successful coating with mesoporous silica.[26–28]

X-ray diffraction (XRD) analysis further confirms the full reduction of α-Fe_2O_3@m-SiO_2 to the Fe_3O_4 phase. Five strong diffraction peaks are observed in the spectrum at 35.4°, 43.0°,

Open Access Article. Published on 01 December 2025. Downloaded on 4/5/2026 1:17:45 AM.
This article is licensed under a Creative Commons Attribution-NonCommercial 3.0 Unported Licence.

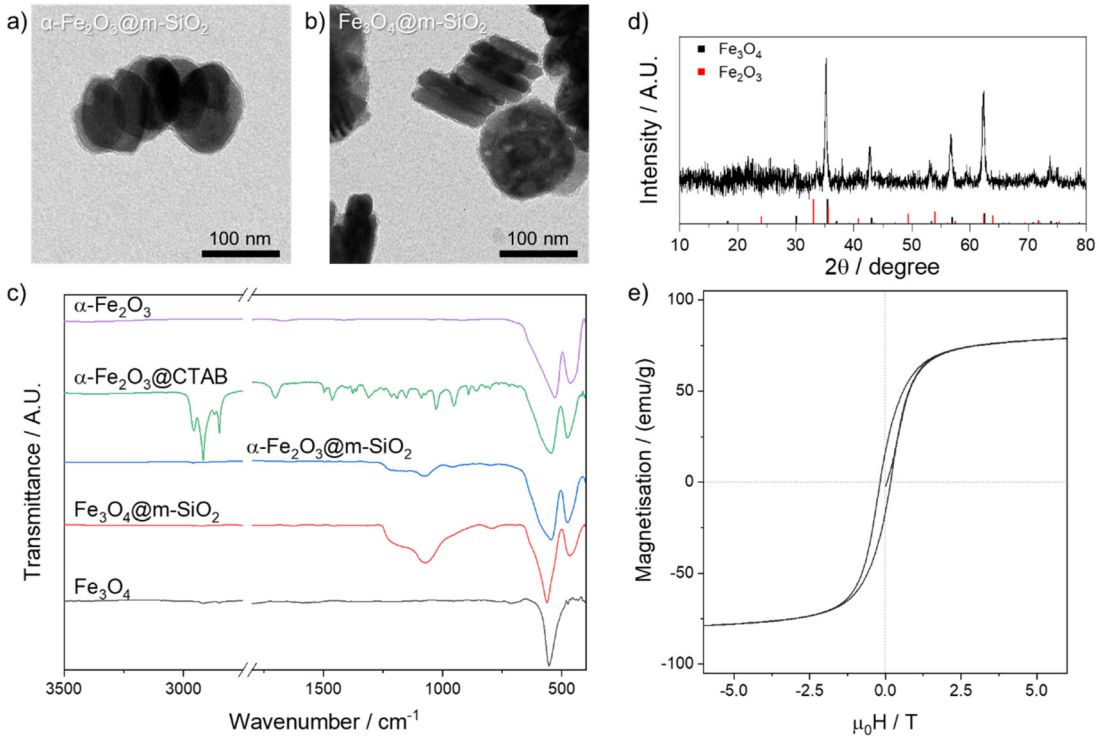

Fig. 3 TEM images (a) of α-Fe_2O_3@m-SiO_2 and (b) Fe_3O_4@m-SiO_2. (c) XRD of Fe_3O_4@m-SiO_2 with the diffraction lines indicating the α-Fe_2O_3 and Fe_3O_4 phases. (d) FTIR spectra of different stages of the sample before and after reduction. Fe_3O_4 is added as the reference. (e) Room temperature magnetization curves of Fe_3O_4@m-SiO_2.

53.4°, 56.9°, and 62.5°, corresponding to the (311), (400), (422), (511), and (440) crystalline planes attributed to the Fe_3O_4 phase (Fig. 3c). XPS quantitative analysis of Fe_3O_4@m-SiO_2 reveals a low total atomic percentage of iron, at 1.76%, consistent with the shallow XPS probing depth of ~5 nm. Nonetheless, the Fe 3p and Fe $2p_{3/2}$ signals are clearly detectable (Fig. S8).[29] The Fe 3p component at 55.5 eV is assigned to the Fe–Si bond, while the O 1s spectrum shows a component at 530.2 eV attributable to the Fe–O–Si interfacial bonds.[30] A second component at 532.9 eV is assigned to the SiO_2 environment, in agreement with the Si $2p_{3/2}$ core peak at 103.7 eV.

FTIR spectroscopy (Fig. 3d) provides further evidence of successful shell formation and reduction. Prior to silica coating, α-Fe_2O_3 exhibits characteristic stretching vibrations at 463 and 530 cm^{-1} (purple line).[31] After complexation with CTAB and before the ethanol/water washing, additional bands appear that can be attributed to trapped surfactant and unreacted reactants within the pores of α-Fe_2O_3@m-SiO_2 (green line). These bands fully disappear after the ethanol/water washing, while the Fe–O stretching bands shift to 476 and 547 cm^{-1} (blue line). These bands are shifted to higher wavenumbers because of the vibration modes of SiO_2. The shift at 476 nm is linked to the asymmetric stretching of Si–O,[32] while the band at 547 cm^{-1} is affected by the Fe–O–Si bending vibration. Additional Si–O bands are observed at 794, 977, 1073, and 1195 cm^{-1}.[32] Finally, the characteristic Fe–O stretching of Fe_3O_4 is slightly shifted in Fe_3O_4@m-SiO_2, from 551 cm^{-1} to 561 cm^{-1}, also due to the contribution of Fe–O–Si.[33] A band near ~475 cm^{-1} is also present, corresponding to the Si–O–Si bending vibration.[34]

The size distribution from TEM micrographs shows that α-Fe_2O_3@m-SiO_2 nanodiscs have an average diameter of around 112 ± 11 nm (Fig. S9), while the average diameter for the Fe_3O_4@m-SiO_2 nanodiscs is 110 ± 14 nm (Fig. S10).

The intensity-weighted DLS size distribution of α-Fe_2O_3 templates dispersed in ethanol exhibits a cumulant hydrodynamic diameter (*z*-average) of ~199 nm, exceeding the dimensions determined by electron microscopy. This discrepancy reflects the partial particle aggregation in suspension. Following the growth of the mesoporous silica, the average hydrodynamic diameter increases to 230 nm. After reduction, Fe_3O_4@m-SiO_2 exhibits further increase with a hydrodynamic average diameter of 451 nm, accompanied by increased PDI (0.42 *vs.* 0.11 for α-Fe_2O_3@m-SiO_2). While Fe_3O_4@m-SiO_2 nanodiscs exhibit a larger hydrodynamic diameter (~451 nm) relative to uncoated MNDs (~100 nm), this increase is consistent with small aggregates of approximately three to four discs, suggesting limited aggregation rather than extensive clustering. Importantly, the mesoporous silica shell provides improved colloidal stability over time, as will be discussed below.

In addition to stabilising the dispersions, the silica shell does not compromise the intrinsic magnetic properties of the nanodiscs. Hysteresis curves recorded at room temperature

This journal is © The Royal Society of Chemistry 2026

Open Access Article. Published on 01 December 2025. Downloaded on 4/5/2026 1:17:45 AM.
This article is licensed under a Creative Commons Attribution-NonCommercial 3.0 Unported Licence.

(Fig. 3e) show that Fe_3O_4@m-SiO_2 retains a saturation magnetization (M_s) of 83.96 emu g^{-1} (Fig. 3e), corresponding to 97.6% of the bulk Fe_3O_4 value (86 emu g^{-1} at 300 K),[35] and higher than previously reported values for ~100 nm Fe_3O_4 nanodiscs with $M_s \approx 80$ emu g^{-1}.[3] These findings demonstrate that the mesoporous silica coating improves colloidal stability without significantly diminishing magnetic performance.

Surface modification *via* polymer grafting

Considering potential biomedical applications of the MNDs, we employed a synthetic strategy designed to grow a polymeric shell through covalent bonding between the inorganic cores and a polymer matrix. This covalent approach was chosen over physical interactions to ensure chemically stable attachment, minimizing the risk of detachment of the nanoparticle coating in complex biological environments and preserving colloidal stability. The synthetic route involves two main steps: first, Fe_3O_4@m-SiO_2 nanoparticles were functionalized with a silane bearing a terminal vinyl group (MEMO). Subsequently, a free-radical precipitation/dispersion polymerization was carried out under ultrasonication using an SDS as a stabilizing agent and an APS/TEMED system to initiate the polymerization. The silanization reaction was optimized to proceed under continuous ultrasonication in toluene at 70 °C for 30 min. Polymer coatings were then grafted using NIPAM and MAA in three different compositions: pure PNIPAM (Fe_3O_4@m-SiO_2@P1), and copolymers of NIPAM and MAA (P(NIPAM-*co*-MAA)), with monomer ratios of 80 : 20 (Fe_3O_4@m-SiO_2@P2) and 50 : 50 (Fe_3O_4@m-SiO_2@P3).

TEM micrographs (Fig. 4a–c) revealed that the polymer shell around MNDs exhibits a smoother appearance, with no clear contrast between silica and the organic material, suggesting that the polymer could have grown within the mesoporous structure of the silica. Gaussian fitting of the shell thickness (Fig. 4d and e) gives values of 6.1 ± 1.4 nm, 7.3 ± 1.5 nm, and 7.5 ± 1.7 nm for Fe_3O_4@m-SiO_2@P1, P2, and P3, respectively, while Fe_3O_4@m-SiO_2 shows a thickness of 3.4 ± 0.8 nm. Statistical analysis using one-way ANOVA followed by Dunnett's multiple comparison test confirms a significant increase in thickness for polymer-coated samples compared to the bare m-SiO_2 layer ($P < 0.0001$) (Table S2).

AFM analysis further highlights morphological changes of the mesoporous silica-coated magnetite nanodiscs after polymer functionalization (Fig. S6 and S11). The hexagonal platelet topography of Fe_3O_4@m-SiO_2 is replaced by large, densely packed plateaus on the surface of polymer-coated nanodiscs. Phase contrast imaging suggests that while silica-coated MNDs exhibit rigid, homogeneous surfaces, polymer-coated MNDs exhibit smoother profiles with increased apparent height and heterogeneous phase responses, indicative of viscoelastic dissipation.

The successful anchoring of the silane was confirmed by FTIR spectroscopy through the appearance of a characteristic carbonyl stretching vibration at around 1720 cm^{-1}. Additionally, the presence of the polymer shell was verified by the appearance of the amide I (mainly due to the C=O stretching vibration) and amide II (a combination of the N–H bending vibration and C–N) bands of PNIPAM, typically observed around 1650 cm^{-1} and 1540 cm^{-1}, respectively.

The colloidal stability of the hybrid nanostructures with different polymers (varying monomer ratios in the P(NIPAM-MAA) copolymer) in water was evaluated by monitoring the average hydrodynamic diameter over time *via* DLS (Fig. 4h). The bare Fe_3O_4 (magenta) initially exhibits an average size of 538 ± 24 nm which increases after 70 min to 1130 ± 131 nm (109% increase), indicating particle aggregation over time. Fe_3O_4@m-SiO_2 shows improved stability, increasing from 490 ± 20 nm up to 725 ± 200 nm (48% increase) after the same time period. Fe_3O_4@m-SiO_2@P1 nanostructures exhibit an initial average size of 480 ± 13 nm, which increases over time to reach 942 nm at 50 min, and then decreases to 719 ± 157 nm after 70 min (corresponding to an overall increase of ~50%). Fe_3O_4@m-SiO_2@P2 and P3 composed of the copolymer P(NIPAM-*co*-MAA) in a ratio of 80 : 20 and 50 : 50, respectively, consistently show smaller hydrodynamic diameters across all time points compared with P1 (PNIPAM alone) and the inorganic nanostructures. The hydrodynamic diameter varies from 436 ± 11 nm to 472 ± 24 nm for Fe_3O_4@m-SiO_2@P2, and 386 ± 23 nm to 410 ± 17 nm for Fe_3O_4@m-SiO_2@P3. Furthermore, the size variation between the initial measurement and the final time point (70 min) for P2 is only around 36 nm (8% increase), and for P3 is around 24 nm (6% increase), highlighting their improved colloidal stability. This behavior is attributed to the negatively charged MAA units, as evidenced by the negative Zeta potential values (Table S1), which enhance electrostatic repulsion and thereby more effectively prevent nanoparticle aggregation in water.

The stability of the MNDs with different coatings was evaluated in RPMI 1640 medium (Roswell Park Memorial Institute 1640), used here as a model of physiological conditions (Fig. 4i). Both Fe_3O_4 and Fe_3O_4@m-SiO_2 show a high degree of aggregation over 70 min, with hydrodynamic diameters increasing from 489 ± 1 nm to 2430 ± 511 nm (397%), and 652 ± 20 nm to 2290 ± 115 nm (251%), respectively, indicating that the silica coating alone is insufficient to prevent agglomeration in biological media. Fe_3O_4@m-SiO_2@P1 behaves similarly to its behavior in water (Fig. 4e), increasing from 507 ± 35 nm to 614 ± 109 nm (21% increase), even reaching values up to 891 ± 68 nm. This demonstrates that PNIPAM, a neutral polymer, provides limited protection against aggregation, although better than Fe_3O_4@m-SiO_2. In contrast, Fe_3O_4@m-SiO_2 coated with P2 and P3 maintain improved colloidal stability than P1 in RPMI medium, with hydrodynamic diameter increasing from 330 ± 5 nm to 595 ± 34 nm (80% increase), and from 424 ± 33 nm to 545 ± 198 nm (29% increase), respectively, over the same time period. Notably, P2 exhibits lower hydrodynamic diameters in RPMI than P3 in water, highlighting its enhanced ability to prevent aggregation under physiological conditions. Moreover, hybrid P2-coated nanostructures consistently show lower PDI values in RPMI medium throughout the entire measurement period, remaining below 0.45 (Fig. S12).

Open Access Article. Published on 01 December 2025. Downloaded on 4/5/2026 1:17:45 AM.
This article is licensed under a Creative Commons Attribution-NonCommercial 3.0 Unported Licence.

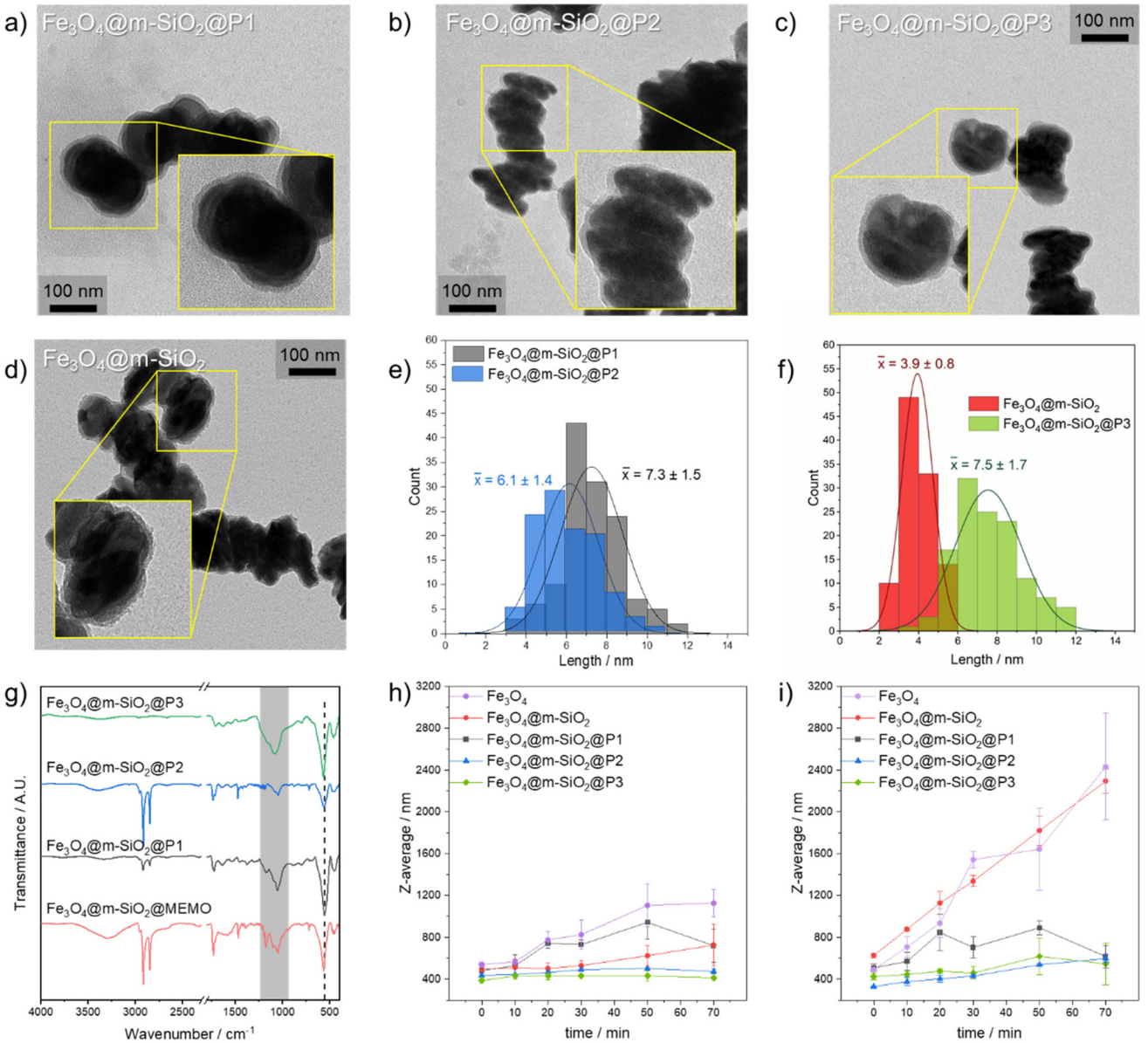

Fig. 4 TEM images of (a) Fe_3O_4@m-SiO_2@P1, (b) Fe_3O_4@m-SiO_2@P2, (c) Fe_3O_4@m-SiO_2@P3 and (d) Fe_3O_4@m-SiO_2 including magnification of selected nanodiscs. Width distribution of the coatings measured from multiple TEM images for (e) Fe_3O_4@m-SiO_2@P1 and Fe_3O_4@m-SiO_2@P2, and (f) Fe_3O_4@m-SiO_2@P3 and Fe_3O_4@m-SiO_2. (g) FTIR spectra showing the silane functionalization, followed by polymerization and purification for the different polymer compositions: P1 corresponds to PNIPAM, P2 to P(NIPAM-*co*-MAA) 80 : 20, and P3 to P(NIPAM-*co*-MAA) 50 : 50. Temporal evolution of particle size measured by DLS, showing the average hydrodynamic diameter of the nanomaterials at different time points in (h) water and (i) RPMI.

Cytotoxicity assay

Since nanodiscs are intended for biological applications, their cytotoxicity was evaluated. *In vitro* cytotoxicity of Fe_3O_4@m-SiO_2 and Fe_3O_4@m-SiO_2@P3 was assessed using WI-38 fibroblasts and HEK-293T (Fig. S13). Fe_3O_4@m-SiO_2@P3 was selected because these nanodiscs showed the highest stability both in water and in cell medium. Non-toxicity is considered as higher than 80% cell viability, according to ISO 10993-5, while 80%–60% is weak, 60%–40% is moderate, and below 40% is strong cytotoxicity.[36] Fe_3O_4@m-SiO_2@P3 showed no signs of cytotoxicity as cell viability remained above the 80% threshold at all evaluated time points and concentrations for both HEK-293T and WI-38. Fe_3O_4@m-SiO$_2$ without polymer coating$_2$ exhibits cytotoxicity in HEK-293T at concentrations of 25 μg mL^{-1} and higher. In contrast, no toxicity is shown for Fe_3O_4@m-SiO to WI-38 cells.

Discussion

During the reduction of hematite, aggregation is likely to take place upon conversion to magnetite as dipole–dipole inter-

This journal is © The Royal Society of Chemistry 2026

Open Access Article. Published on 01 December 2025. Downloaded on 4/5/2026 1:17:45 AM.
This article is licensed under a Creative Commons Attribution-NonCommercial 3.0 Unported Licence.

actions of closely packed MNDs become prevalent over vortex magnetization, which is detrimental for applications in biological environments. Here, we have explored strategies to improve the colloidal stability of MNDs, particularly under physiological conditions.

First, oleic acid (OA) was evaluated as a stabilizing agent during reduction. TEM analysis revealed the erosion of the material, showing small spheres alongside the MNDs, attributed to successive cycles of dissolution and reprecipitation of iron oxide from the discs under harsh reaction conditions.[37,38] DLS measurements both in water and ethanol showed no significant differences between the MNDs reduced in the presence or absence of OA. XPS and FTIR spectra further confirmed minimal OA adsorption. These results suggest that OA is inefficiently adsorbed on the MNDs during the reduction process, possibly due to surface-bound acetate ions that block binding.

To mitigate aggregation, applying a silica coating on the Fe_3O_4 surface should provide a physical barrier preventing direct contact between MNDs and reducing magnetic dipole interactions that dominate after reduction. As evidenced by the DLS size distribution analysis, hematite exhibits a lower tendency to aggregate than magnetite; therefore, silica coating was applied to the hematite template prior to reduction. A mesoporous layer of silica is preferable over a hard silica coating because the large pore area available in the mesoporous layer enables H_2 to freely flow through the silica layer reaching the hematite template for reduction. The successful mesoporous shell formation was confirmed by TEM, XPS, FTIR and AFM analyses and the efficient reduction within 30 min to the Fe_3O_4 phase was demonstrated by the saturation magnetization and XRD spectrum showing the presence of a pure magnetite crystalline phase with high M_s values.

The silica layer remains chemically and morphologically stable after the reduction step, with a slight decrease in thickness from 6 nm in hematite to 4 nm in magnetite as evidenced by FTIR, XPS and TEM analyses. DLS measurements show that Fe_3O_4@m-SiO_2 nanodiscs exhibit significantly less aggregation in water than uncoated MNDs over time. While uncoated Fe_3O_4 suffered an increment in hydrodynamic diameter of 109% (538 nm to 1130 nm) over 70 min, the mesoporous silica-coated material, Fe_3O_4@m-SiO_2, showed a much higher degree of stabilization, with only a 48% increase in hydrodynamic diameter (490 nm to 725 nm). However, in RPMI medium, both Fe_3O_4 and Fe_3O_4@m-SiO_2 show increments in size of 397% (489 nm to 2430 nm) and 266% (625 nm to 2290 nm) over 70 min, respectively, in agreement with the reported behavior of silica nanoparticles in this medium.[39]

The mesoporous silica coating also offers great versatility for surface functionalization. Its surface can be readily modified with silane groups, and the mesoporous structure increases the surface area available for covalent attachment of these molecules. Using this approach, we grafted NIPAM/MAA copolymers onto the porous silica coating.

MNDs@m-SiO_2 with PNIPAM coating exhibited larger hydrodynamic diameters over time compared to Fe_3O_4@m-SiO_2 alone. Nonetheless, this polymer grafting leads to a higher degree of stabilization in RPMI medium compared to both uncoated MND and the m-SiO_2 coated MNDs. Polymer coatings P2 and P3 (containing 20% and 50% MAA, respectively) showed improved stability up to 70 min in both water and cell media, with increases in hydrodynamic diameter of 8% (436 nm to 472 nm) and 6% (386 nm to 410 nm) in water and 80% (330 nm to 595 nm) and 29% (424 nm to 545 nm) in RPMI medium.

Although the colloidal stability of P2 and P3 coated MNDs is better in water than in RPMI media, these hybrids exhibit lower size distribution in both environments compared with the MNDs and MNDs@m-SiO_2. Hybrid nanostructures with P2 coating show an increase in hydrodynamic diameter of approximately threefold smaller than that of bare inorganic MNDs in water and about fivefold smaller in cell culture media. These results demonstrate that negatively charged MAA monomers effectively prevent aggregation under physiological conditions.

Finally, cytotoxicity evaluation of Fe_3O_4@m-SiO_2 and Fe_3O_4@m-SiO_2@P3 was performed with WI-38 fibroblasts and HEK-293T cells. Fe_3O_4@m-SiO_2@P3 showed no cytotoxicity at any of the tested concentrations, even at 200 μg mL^{-1}, for both cell lines. Fe_3O_4@m-SiO_2 was only observed to be cytotoxic (cell viability lower than 80%) for HEK-293T cells at concentrations higher than 12.5 μg mL^{-1}. These results hint at a positive effect of the polymer coating on decreasing toxicity, which may be related to a lower cellular uptake of the polymer coated nanodiscs. Further studies on cell uptake and the intracellular fate of nanodiscs are on the way.

Overall, applying a mesoporous silica shell to hematite templates allows complete reduction to magnetite while physically reducing aggregation, and subsequent silanization and polymer grafting significantly improve colloidal stability in both aqueous and biologically relevant environments.

Conclusions

We have improved the synthesis of MNDs by removing the unnecessary and potentially detrimental addition of OA from the wet-reduction process. Hematite templates were successfully coated with a thin mesoporous silica shell, which reduced aggregation while allowing efficient reduction to magnetite, yielding nanodiscs with magnetic properties comparable to those of uncoated magnetite. The mesoporous silica coating alone improved colloidal stability in water when contrasted with uncoated MNDs but was insufficient to prevent aggregation in cell culture media. Subsequent functionalization of the mesoporous silica shell with negatively charged NIPAM/MAA copolymers (P2 and P3) further enhanced colloidal stability in cell culture media. Over 70 min, the size increase of hybrid nanostructures with P2 coating is approximately threefold smaller than that of bare inorganic MNDs in water and about fivefold smaller in cell culture media.

Open Access Article. Published on 01 December 2025. Downloaded on 4/5/2026 1:17:45 AM. This article is licensed under a Creative Commons Attribution-NonCommercial 3.0 Unported Licence.

Author contributions

P. R. D.: investigation, data curation, methodology, conceptualization, writing – original draft, and writing – review & editing. M. A. M.: investigation, data curation, supervision, and writing – review & editing. E. K.: investigation: F. W.: investigation. V. D. T.: investigation and supervision. S. M. I.: investigation. E. G. P.: investigation and data curation. S. T.: investigation. D. G.: funding acquisition, conceptualization, supervision, and writing – review & editing. S. E. M.: funding acquisition, conceptualization, supervision, writing – original draft, and writing – review & editing.

Conflicts of interest

There are no conflicts of interest to declare.

Data availability

Data for this article are available at Zenodo, https://zenodo.org/uploads/17090464.

Supplementary information (SI) is available. Supplementary information includes additional characterization of magnetic nanodiscs and coatings: DLS, TEM, XPS, AFM, EDX data; and the toxicity evaluation of MNDs in two cell lines. See DOI: https://doi.org/10.1039/d5nr03822g.

Acknowledgements

S. E. M. and D. G. acknowledge the funding from the European Innovation Council Pathfinder Challenge project, BRAINSTORM (GA 101099355). D. G. acknowledges ERC Starting Grant BRAINMASTER (GA 101116410). S. E. M. thanks the PID2020-114356RB-I00 project from the Ministry of Science and Innovation of the Government of Spain. We gratefully acknowledge the support of Dr Paula C. Angelomé for helpful advice on mesoporous coatings. S. E. M. and D. G. are thankful to the FAU Visiting Professorship Program which enabled discussions, conceptualization, and collaborative work on this project. The authors gratefully acknowledge the support of Prof. Dr Karsten Meyer (Friedrich-Alexander-Universität Erlangen-Nürnberg) for providing SQUID magnetometer data and Prof. Dr Julien Bachmann (Friedrich-Alexander-Universität Erlangen-Nürnberg) for providing access to XRD.

References

1 T. Potrč, S. Kralj, S. Nemec, P. Kocbek and M. E. Kreft, *Nanoscale*, 2023, **15**, 8611–8618.
2 Z. Ma, J. Mohapatra, K. Wei, J. P. Liu and S. Sun, *Chem. Rev.*, 2023, **123**, 3904–3943.
3 Y. Yang, M. Li, Y. Wu, B. Zong and J. Ding, *RSC Adv.*, 2016, **6**, 25444–25448.
4 J. Bao, S. Guo, X. Zu, Y. Zhuang, D. Fan, Y. Zhang, Y. Shi, Z. Ji, J. Cheng and X. Pang, *Front. Bioeng. Biotechnol.*, 2021, **9**, 721617.
5 V. R. R. Aquino, J. C. R. Aquino, J. A. H. Coaquira, A. F. Bakuzis, M. H. Sousa and P. C. Morais, *Mater. Des.*, 2023, **232**, 112082.
6 H. Mamiya, H. Fukumoto, J. L. C. Huaman, K. Suzuki, H. Miyamura and J. Balachandran, *ACS Nano*, 2020, **14**, 8421–8432.
7 S. A. Hescham, P. H. Chiang, D. Gregurec, J. Moon, M. G. Christiansen, A. Jahanshahi, H. Liu, D. Rosenfeld, A. Pralle, P. Anikeeva and Y. Temel, *Nat. Commun.*, 2021, **12**, 1–10.
8 D. Gregurec, A. W. Senko, A. Chuvilin, P. D. Reddy, A. Sankararaman, D. Rosenfeld, P. H. Chiang, F. Garcia, I. Tafel, G. Varnavides, E. Ciocan and P. Anikeeva, *ACS Nano*, 2020, **14**, 8036–8045.
9 H. M. Fan, J. B. Yi, Y. Yang, K. W. Kho, H. R. Tan, Z. X. Shen, J. Ding, X. W. Sun, M. C. Olivo and Y. P. Feng, *ACS Nano*, 2009, **3**, 2798–2808.
10 M. Zhu, Y. Wang, D. Meng, X. Qin and G. Diao, *J. Phys. Chem. C*, 2012, **116**, 16276–16285.
11 J. Zhou, D. Song, S. T. Mergelsberg, Y. Wang, N. M. Adhikari, N. Lahiri, Y. Zhao, P. Chen, Z. Wang, X. Zhang and K. M. Rosso, *Sci. Adv.*, 2024, **10**, DOI: 10.1126/sciadv.adi7494.
12 Y. Wang, S. Xue, Q. Lin, D. Song, Y. He, L. Liu, J. Zhou, M. Zong, J. J. De Yoreo, J. Zhu, K. M. Rosso, M. L. Sushko and X. Zhang, *Proc. Natl. Acad. Sci. U. S. A.*, 2022, **119**, e2112679119.
13 C. Gao, F. Lyu and Y. Yin, *Chem. Rev.*, 2021, **121**, 834–881.
14 A. Guerrero-Martínez, J. Pérez-Juste and L. M. Liz-Marzán, *Adv. Mater.*, 2010, **22**, 1182–1195.
15 Z. Tian, X. Yu, Z. Ruan, M. Zhu, Y. Zhu and N. Hanagata, *Microporous Mesoporous Mater.*, 2018, **256**, 1–9.
16 W. Zhao, J. Gu, L. Zhang, H. Chen and J. Shi, *J. Am. Chem. Soc.*, 2005, **127**, 8916–8917.
17 A. Adam and D. Mertz, *Nanomaterials*, 2023, **13**, 1342.
18 J. M. Rosenholm, J. Zhang, W. Sun and H. Gu, *Microporous Mesoporous Mater.*, 2011, **145**, 14–20.
19 M. A. Macchione, C. Biglione and M. Strumia, *Polymers*, 2018, **10**, 527.
20 M. A. Macchione, D. A. Bedoya, E. Rivero-Buceta, P. Botella and M. C. Strumia, *Nanomaterials*, 2022, **12**, 3835.
21 L. Chen, X. Yang, J. Chen, J. Liu, H. Wu, H. Zhan, C. Liang and M. Wu, *Inorg. Chem.*, 2010, **49**, 8411–8420.
22 L. Zhang, R. He and H. C. Gu, *Appl. Surf. Sci.*, 2006, **253**, 2611–2617.
23 M. Masuku, L. Ouma and A. Pholosi, *Environ. Nanotechnol., Monit. Manage.*, 2021, **15**, 100429.
24 H. Kaur, S. Chaudhary, H. Kaur, M. Chaudhary and K. C. Jena, *ACS Appl. Nano Mater.*, 2022, **5**, 411–422.

 This journal is © The Royal Society of Chemistry 2026

Open Access Article. Published on 01 December 2025. Downloaded on 4/5/2026 1:17:45 AM.
This article is licensed under a Creative Commons Attribution-NonCommercial 3.0 Unported Licence.

25 J. Kim, J. E. Lee, J. Lee, J. H. Yu, B. C. Kim, K. An, Y. Hwang, C. H. Shin, J. G. Park, J. Kim and T. Hyeon, *J. Am. Chem. Soc.*, 2006, **128**, 688–689.
26 E. Y. Trofimova, D. A. Kurdyukov, Y. A. Kukushkina, M. A. Yagovkina and V. G. Golubev, *Glass Phys. Chem.*, 2011, **37**, 378–384.
27 D. R. Streltsov, K. M. Borisov, A. A. Kalinina and A. M. Muzafarov, *Nanomaterials*, 2023, **13**, 1–23.
28 E. A. Sosnov, T. S. Trubina, D. A. Kurdyukov and A. A. Malygin, *Glass Phys. Chem.*, 2019, **45**, 365–371.
29 T. Radu, C. Iacovita, D. Benea and R. Turcu, *Appl. Surf. Sci.*, 2017, **405**, 337–343.
30 A. Glaria, S. Soulé, N. Hallali, W. S. Ojo, M. Mirjolet, G. Fuks, A. Cornejo, J. Allouche, J. C. Dupin, H. Martinez, J. Carrey, B. Chaudret, F. Delpech, S. Lachaize and C. Nayral, *RSC Adv.*, 2018, **8**, 32146–32156.
31 L. Hu, A. Percheron, D. Chaumont and C. H. Brachais, *J. Sol-Gel Sci. Technol.*, 2011, **60**, 198–205.
32 H. L. Ding, Y. X. Zhang, S. Wang, J. M. Xu, S. C. Xu and G. H. Li, *Chem. Mater.*, 2012, **24**, 4572–4580.
33 M. Ishii, M. Nakahira and T. Yamanaka, *Solid State Commun.*, 1972, **11**, 209–212.
34 Z. Shahbazarab, M. Nasr-Esfahani and M. Montazerozohori, *React. Chem. Eng.*, 2025, **10**, 2386–2397.
35 Y. Hadadian, H. Masoomi, A. Dinari, C. Ryu, S. Hwang, S. Kim, B. K. Cho, J. Y. Lee and J. Yoon, *ACS Omega*, 2022, **7**, 15996–16012.
36 ISO 10993-5, Int. Organ. Stand.
37 W. W. Yu, J. C. Falkner, C. T. Yavuz and V. L. Colvin, *Chem. Commun.*, 2004, 2306–2307.
38 T. Wijakmatee, Y. Shimoyama and Y. Orita, *Langmuir*, 2023, **39**, 9253–9261.
39 A. Saorin, A. Martinez-Serra, G. J. Paparoni-Bruzual, M. Crozzolin, V. Lombardi, M. Back, P. Riello, M. P. Monopoli and F. Rizzolio, *Mater. Adv.*, 2024, **5**, 5106–5117.